*R*esearch in
*A*stronomy and
*A*strophysics

Spectral deconvolution analysis on Olivine-Orthopyroxene mixtures with simulated space weathering modifications

Hui-Jie Han (韩慧杰)[1], Xiao-Ping Lu (卢晓平)[1⋆], Te Jiang (姜特)[2], Chih-Hao Hsia (夏志浩)[1,3], Ya-Zhou Yang (杨亚洲)[4], Peng-Fei Zhang (张鹏飞)[1] and Hao Zhang (张昊)[2,5]

[1] State Key Laboratory of Lunar and Planetary Sciences, Macau University of Science and Technology, Taipa 999078, Macau, China; *xplu@must.edu.mo*
[2] Planetary Science Institute, School of Earth Sciences, China University of Geosciences, Wuhan 430074, China
[3] CNSA Macau Center for Space Exploration and Science, Taipa 999078, Macau, China
[4] State Key Laboratory of Space Weather, National Space Science Center, Chinese Academy of Sciences, Beijing 100190, China
[5] CAS Center for Excellence in Comparative Planetology, Hefei 230026, China

Abstract Olivine and pyroxene are important mineral end-members for studying the surface material compositions of mafic bodies. The profiles of visible and near-infrared spectra of olivine-orthopyroxene mixtures systematically vary with their composition ratios. In our experiments, we combine the RELAB spectral database with new spectral data obtained from some assembled olivine-orthopyroxene mixtures. We found that the commonly-used band area ratio (BAR, Cloutis et al.) does not work well on our newly obtained spectral data. To investigate this issue, an empirical procedure based on fitted results by a modified Gaussian model is proposed to analyze the spectral curves. Following the new empirical procedure, the end-member abundances can be estimated with a 15% accuracy with some prior mineral absorption features. In addition, the mixture samples configured in our experiments are also irradiated by pulsed lasers to simulate and investigate the space weathering effects. Spectral deconvolution results confirm that low-content olivine on celestial bodies is difficult to measure and estimate. Therefore, the olivine abundance of space weathered materials may be underestimated from remote sensing data. This study may be utilized to quantify the spectral relationship of olivine-orthopyroxene mixtures and further reveal their correlation between the spectra of ordinary chondrites and silicate asteroids.

Key words: techniques: spectroscopic — instrumentation: spectrographs — methods: data analysis — minor planets, asteroids: general

1 INTRODUCTION

The spectral absorption features provided by hyperspectral remote sensing enable us to investigate the geological and geochemical information over the imaged area (Cloutis 1996; Clark et al. 2003; Zaini et al. 2014). Generally, these spectral features can be exploited to identify the minerals, rocks, water (ices) and organic materials on celestial bodies (Adams 1974; Singer 1981; Burbine et al. 2002; Pieters et al. 2009; Basilevsky et al. 2012; Roush et al. 2015; Lauretta et al. 2019), such as terrestrial planets, moons and asteroids (Cloutis & Bell 2000; Ohtake et al. 2009; Lindsay et al. 2015; Zhang et al. 2015; Hu et al.

2019; Tsuda et al. 2020). Visible and near-infrared (VNIR) reflectance spectra are susceptible to mafic minerals (Pieters & Mustard 1988; Lucey 2004; Staid et al. 2011), which contain the characteristics of mineral composition and crystal structure (Hunt 1977; Mustard et al. 2005). As the major group of mafic minerals, olivine and pyroxene are important materials in understanding geologic evolution, the differentiation process and cooling history of terrestrial bodies (Wells 1977; Ishii et al. 1983; Cloutis & Gaffey 1991; Klima et al. 2011). However, many limiting factors should be considered when using reflectance spectra to analyze remote sensing data from airless bodies, because most reflectance spectra collected under laboratory conditions are not consistent with the

⋆ Corresponding author

Table 1 Chemical Compositions of These Olivine and Orthopyroxene Samples

Sample ID	AG-TJM-008	AG-TJM-009	PO-CMP-017	PE-CMP-012	OWN-OLV	OWN-OPX
Mineral	Olivine	Hypersthene	Olivine	Enstatite	Olivine	Enstatite
SiO_2	40.81	54.09	40.87	55.3	40.66	52.06
TiO_2	0	0.16	0	0.05	0.011	0.13
Al_2O_3	0	1.23	0.01	0.12	0.34	4.1
Cr_2O_3	0	0.75	0.04	0	0	0
Fe_2O_3	0	0	0	0	9.76	7.44
FeO	9.55	15.22	7.77	9.38	0	0
MnO	0.14	0.49	0.14	0.15	0.11	0.13
MgO	49.42	26.79	51.58	32.8	48.00	34.85
CaO	0.05	1.52	0.03	0.45	0.056	0.98
Na_2O	0	0.05	0.01	0	0.008	0.13
K_2O	0	0.05	0	0.02	0.004	0.006
P_2O_3	0	0	0	0.01	0.005	0.016
H_2O	0	0	0	0	0.04	0.04
Text	Fo 90.5 Fa 9.5	En 73.6 Fs 23.4 Wo 3.0	Fo 92.2 Fa 7.8	En 85.5 Fs 13.7 Wo 0.8	Fo 89.8 Fa 10.2	En 87.7 Fs 10.5 Wo 1.8

The number unit is wt. %.

data by remote sensing (Bishop et al. 1998; Cloutis et al. 2008; Shirley & Glotch 2019). One thing that needs to be focused on is "space weathering" which can change the chemical compositions and optical properties of the surface materials (Pieters et al. 2000; Brunetto et al. 2006; Fu et al. 2012). It can make the spectral curves redden and darken, and difficult to identify and interpret (Hapke 2001; Chapman 2004; Han et al. 2020). Therefore, many methods for space weathering spectral deconvolution are extensively studied in order to derive accurate data interpretation (Sunshine & Pieters 1993, 1998; Gallie et al. 2008; Han et al. 2020; Potin et al. 2020).

1.1 Olivine, Pyroxene and Their Mixture Spectroscopy

Olivine is typically the dominant and foremost mineral crystallizing from liquid magma in the Earth's mantle and bears rich information about the magma ocean (Elthon 1979; Garcia et al. 1995; Danyushevsky et al. 2000; Dyar et al. 2009). Olivines are mafic silicates with the formula $(Mg, Fe)_2SiO_4$, which are solid solutions ranging from fayalite (Fe_2SiO_4) to forsterite (Mg_2SiO_4). The olivine structure is nearly hexagonally close-packed and there are two octahedral sites, M1 and M2. Half of the two octahedral interstices is occupied by divalent metal ions, usually either Mg^{2+} or Fe^{2+} (Dyar et al. 2009). The color of olivine is mainly determined by the content of Fe^{2+} content. It looks green with lower content of Fe^{2+} but becomes brown at high iron content. In VNIR reflectance spectra, olivine is characterized by its Fe^{2+} electronic transition absorption bands (Burns 1970; Hunt 1977), and forming a wide and superimposed absorption near the 1.0 μm region (Fig. 1(a)). As the
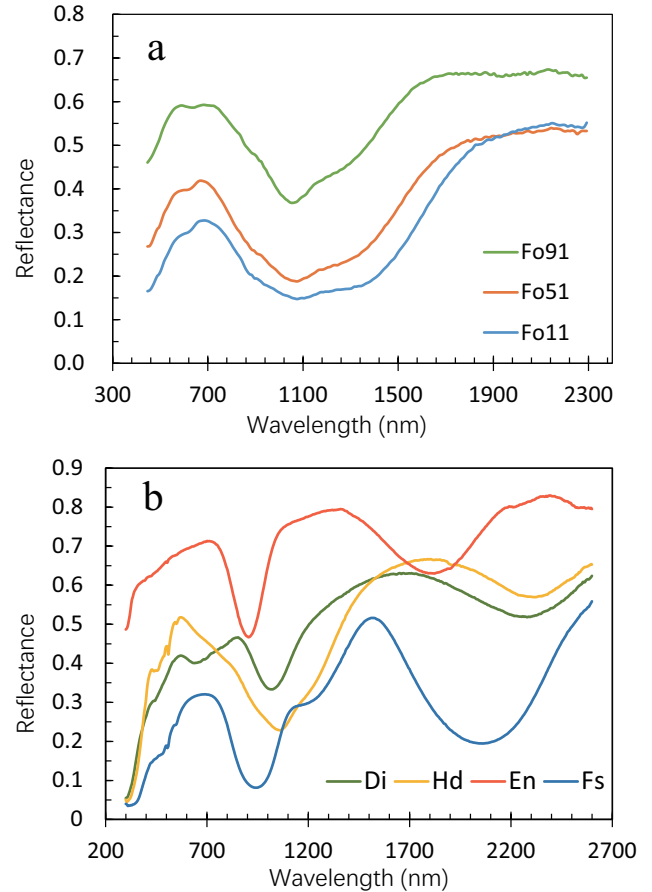

Fig. 1 Reflectance spectra of olivine with varying Mg-number (Fo#) and the ones with pyroxene quadrilateral end-members. (a). Spectra of olivine with varied Fo#. (b). Comparison of the spectra with various pyroxene quadrilateral end-members: Di (*diopside; shown as green*), Hd (*hedenbergite; orange*), En (*enstatite; red*) and Fs (*ferrosillite; blue*)
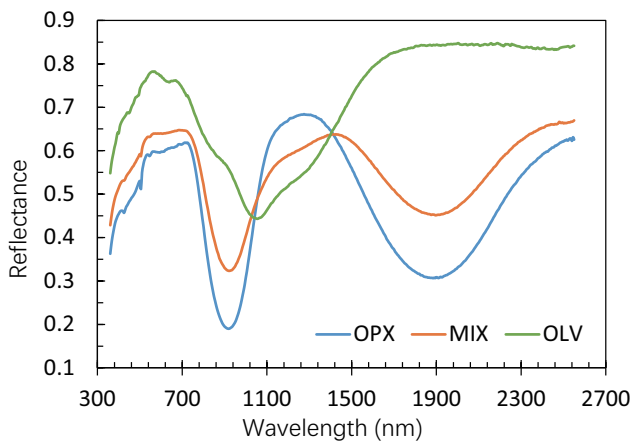
Fig. 2 VNIR reflectance spectra of three mineral components with orthopyroxene (*shown as blue*), olivine (*green*) and olivine-orthopyroxene mixture (*red*). The RELAB IDs of these spectra are AG-TJM-008 (OLV), AG-TJM-009 (OPX) and AG-TJM-019 (MIX) respectively.

Fe^{2+} abundance increases, the 1.0 μm absorption band center shifts toward longer wavelength and the bandwidth increases (Sunshine & Pieters 1998; Han et al. 2020).

Pyroxenes are crystallized from original magma and form the primary component of planetary upper mantle and crust, and bear rich magma information (Elkins-Tanton et al. 2005; Elardo et al. 2011; Head & Wilson 2017). Several geothermobarometric tools have focused on pyroxene to study igneous differentiation in the Earth, asteroids and meteorites (Lindsley 1983; Cloutis & Gaffey 1991; Sunshine et al. 2004; Klima et al. 2008). Pyroxenes are single-chain silicates with the general formula $XYSi_2O_6$, where X and Y are both divalent cations (commonly Ca, Fe, Mg, etc.). The stacking of chains gives rise to two types of cavities, labeled M1 (close to octahedral in shape) and M2 (more irregular in shape) (Burns 1970). Fe^{2+} in the two different crystallographic positions M1 and M2 is responsible for the dominant pyroxene spectral absorptions in the VNIR region, which produce two prominent absorption features near 1.0 μm (Band 1) and 2.0 μm (Band 2) bands. However, substitutions of other cations such as Ca^{2+} change the crystal structure and make the absorption characteristic move towards longer wavelength (Adams 1974; Klima et al. 2011). Furthermore, it was found that in the spectra of pyroxenes (Fig. 1(b)), the wavelengths of the two main absorption bands change as a function of the concentrations of Fe^{2+} and Ca^{2+} (Adams 1974; Klima et al. 2007).

The spectral properties of pyroxenes have been intensively studied in the past (Cloutis & Gaffey 1991; Sunshine & Pieters 1993). The most basic division of pyroxenes is between orthopyroxenes (OPX) and clinopy-

roxenes (CPX) which is based on differences in chemical composition and crystal structure. According to this scheme, orthopyroxenes essentially contain <5 mol% $CaSiO_3$ (wollastonite, Wo) and possess orthorhombic symmetry, while clinopyroxenes can contain $0 \sim 50$ mol% Wo and manifest monoclinic symmetry (Adams 1974; Cloutis & Gaffey 1991). Therefore, they can form a quadrilateral diagram of pyroxenes, in which the corners of the quadrilateral are the pyroxene end-members diopside (Di, $CaMgSi_2O_6$), hedenbergite (Hd, $CaFeSi_2O_6$), enstatite (En, $Mg_2Si_2O_6$) and ferrosilite (Fs, $Fe_2Si_2O_6$). Example spectra are displayed in Figure 1(b). The olivine and pyroxene spectral data are all taken from the Reflectance Experiment Laboratory (RELAB) database supported by Brown University. [1]

According to the information described above, retrieving the mafic mineral features from the obtained reflectance spectra does seem to be a viable task. It provides an effective method for remote analysis of mafic minerals on the planet's surface. However, it is still difficult to directly interpret the spectra because spectral analysis is hampered by the overlapping absorption features, especially when dealing with a mixture of minerals (Clénet et al. 2011). The spectral properties of mineral mixtures do not linearly vary with the relative abundances of different end-members (Adams 1974; Singer 1981; Cloutis & Gaffey 1991).

In this study, we choose the forsterite and low-Fe orthopyroxene as the two end-members. Low-Fe orthopyroxene spectra show a narrow strong absorption near the 0.92 μm region and a wide absorption near the 1.8 to 1.9 μm region (Klima et al. 2007). Therefore, the center positions of these two absorption bands will be important information for studying the olivine-orthopyroxene mixture spectra. Figure 2 features the VNIR reflectance spectra of olivine, orthopyroxene and their mixture (50% OLV + 50% OPX).

1.2 Space Weathering Simulations

The spectra of asteroids and lunar regolith are obviously different from those of the laboratory minerals. The former are characterized by distinct red continua slope and weak absorption unlike those of fresh rocks in the laboratory. Nanophase iron particles ($npFe^0$) have been widely observed in lunar soil which is confirmed to be the cause of the difference in these spectra. It is widely thought that the formation of $npFe^0$ in lunar soil is the result of space weathering, which includes micrometeorite bombardment, energetic particles, as well as cosmic rays (Dybwad 1971; Hapke 1973; Pieters et al. 1993). To

---

[1] *http://www.planetary.brown.edu/relab/*

Table 2 Information Summary on End-member and Synthetic Mixed Samples

Sample ID	OLV : OPX	Sample ID	OLV : OPX	Sample ID	OLV : OPX (Irradiate)
AG-TJM-008	Olivine	AG-TJM-017	1 : 9	XT-TXH-030-P	2.5 : 7.5 (No)
AG-TJM-009	Hypersthene	AG-TJM-018	3 : 7	XT-TXH-031-P	5 : 5 (No)
PO-CMP-017	Olivine	AG-TJM-019	5 : 5	XT-TXH-032-P	7.5 : 2.5 (No)
PE-CMP-012	Enstatite	AG-TJM-014	7 : 3	XT-TXH-030-P1	2.5 : 7.5 (15 mJ)
OWN-OLV	Olivine	AG-TJM-020	9 : 1	XT-TXH-031-P1	5 : 5 (15 mJ)
OWN-OPX	Enstatite	XO-CMP-015	9 : 1	XT-TXH-032-P1	7.5 : 2.5 (15 mJ)
OWN-OL1/EN4	2 : 8	XO-CMP-016	7.5 : 2.5	XT-TXH-030-P2	2.5 : 7.5 (15 mJ * 2)
OWN-OL2/EN3	4 : 6	XO-CMP-017	5 : 5	XT-TXH-031-P2	5 : 5 (15 mJ * 2)
OWN-OL3/EN2	6 : 4	XO-CMP-018	2.5 : 7.5	XT-TXH-032-P2	7.5 : 2.5 (15 mJ * 2)
OWN-OL4/EN1	8 : 2	XO-CMP-019	1 : 9		

Six samples with IDs like OWN-xxxx come from our experiment, with grain size less than 75 µm. The others come from RELAB. Seven samples with IDs like AG-TJM-xxx have grain size < 38 µm. The grain size of the other RELAB samples is 45 ∼ 75 µm. Five samples with IDs like XO-CMP-xxx are olivine-enstatite mixture samples. Nine samples with IDs like XT-TXH-xxx are olivine-bronzite mixture samples, and six of these nine samples are irradiated with a pulsed laser to study the effect of space weathering. The total amount of each mixture is counted as 10.

Table 3 MGM Modeling Parameters of Mixture Sample Spectra

Sample ID		AG-TJM-019		OWN-OL3/EN2	
Abundance		50% OLV + 50% OPX		60% OLV + 40% OPX	
Gaussian Fitting Parameters		Starting Parameters	Final Parameters	Starting Parameters	Final Parameters
Continua	Parameter 1	6.00E-01	6.17E-01	6.60E-01	6.57E-01
	Parameter 2	8.50E-05	8.49E-05	1.10E-05	1.10E-05
	Parameter 3	–2.30E-08	–2.50E-08	–1.50E-08	–1.68E-08
M1-1	Center	840	836.8	840	859.1
	FWHM	150	102.9	150	141.7
	Strength	–0.08	–0.802	–0.07	–0.069
M2	Center	1035	1056.1	1030	1050.0
	FWHM	150	183.6	170	168.6
	Strength	–0.15	–0.152	–0.13	-0.141
M1-2	Center	1245	1221.6	1220	1211.4
	FWHM	300	258.3	320	353.2
	Strength	–0.16	–0.117	–0.15	–0.145
Band 1	Center	920	919.6	920	919.1
	FWHM	200	176.8	200	179.5
	Strength	–0.65	–0.686	–0.20	–0.203
Band 2	Center	1885	1888.5	1800	1800.1
	FWHM	500	541.2	450	439.5
	Strength	-0.40	-0.422	–0.12	–0.114
Root Mean Square Error		2.523E-03		3.588E-03	

Band center and FWHM are in the unit of nanometers. The final parameters are rounded off to proper precision. Band 1 is for absorption near 1.0 µm in OPX, while Band 2 is for absorption near 2.0 µm in OPX.

understand the physical and chemical mechanisms of space weathering, many simulation experiments were conducted in laboratories (e.g., Keller & McKay 1993; Yamada et al. 1999; Hapke 2001; Loeffler et al. 2009; Fu et al. 2012; Jiang et al. 2019). These experiments irradiated different samples with a pulsed laser beam to simulate the irradiation of micrometeorite bombardments; or implanted proton particles (such as H^+, He^+ and Ar^+) onto the samples to simulate solar wind implantation; or heating the samples with a microwave furnace at high temperature in a vacuum to simulate the space environment. Among these methods, pulsed laser irradiation is effective in

generating space weathering effects. Since the pulsed laser can pump energy on a very short time scale, it can be analogous to a high-speed and low-mass dust particle micrometeorite impact (Yamada et al. 1999; Yang et al. 2017). In this study, we utilized pulsed laser irradiation for space weathering simulations.

As an overview of this study, firstly we collected and assembled some olivine-orthopyroxene mixture spectra, and the assembled samples were also irradiated with a pulsed laser in our experiment. Some calculation methods are utilized to study these spectra. These spectral data, experiments and research methods will be presented in

Table 4 Comparisons of the Absorption Band Centers Before and After Irradiations

Sample ID	Original		Irradiated	
	(1 μm)	(2 μm)	(1 μm)	(2 μm)
OWN-OPX	912.16	1795.26	913.45	1803.38
OWN-OL1/EN4	911.52	1801.50	912.16	1805.26
OWN-OL2/EN3	915.38	1804.01	915.38	1809.04
OWN-OL3/EN2	931.16	1824.32	922.55	1808.41
OWN-OL4/EN1	1037.15	1824.32	1041.11	1824.32
OWN-OLV	1056.17	- -	1057.03	- -

Band centers are in nm and values listed in this table are approximations.

Section 2. However, these methods have limitations and do not work well for some samples, so we developed an empirical procedure to deal with these spectral data. The results and some discussions are presented in Section 3. The conclusions are summarized in Section 4.

2 SAMPLES AND EXPERIMENTAL METHODS

2.1 Samples and Reflectance Spectra Measurements

The spectra of synthetic mixtures presented in this study are taken from the RELAB database and our experiment. The end-member components of RELAB synthetic mixture samples are natural olivine (AG-TJM-008) and hypersthene (AG-TJM-009) with grain sizes smaller than 38 μm. The mass mixing ratios of the two minerals are 1/9, 3/7, 5/5, 7/3 and 9/1. Another part of synthetic mixture samples from RELAB is natural olivine (PO-CMP-017) and enstatite (PE-CMO-012) mixtures and the grain size is 45 ∼ 75 μm. The mass mixing ratios of the two minerals are 1/9, 2.5/7.5, 5/5, 7.5/2.5 and 9/1. Chemical compositions of these end-member minerals are listed in Table 1. The reflectance spectra of olivine-hyperthene mixtures are shown in Figure 3(a). In addition, we also utilize some olivine-bronzite mixture samples whose end-member components are not analyzed. The sample IDs and mixture compositions of these samples are listed in Table 2. Measurements of these olivine-orthopyroxene mixtures are conducted using a bidirectional VNIR spectrometer with an incidence angle of 30° and an emission angle of 0° ranging from 0.30 (or 0.32) to 2.55 (or 2.60) μm.

The other part of the samples come from our experiment. We collect some natural pure olivine (OWN-OLV) and enstatite (OWN-OPX) samples as experimental materials. The samples are ground and sieved into grain size less than 75 μm. Chemical compositions of these sample powders are analyzed with a wet chemistry method and listed in Table 1. The mass mixing ratios of the two minerals are 1/4, 2/3, 3/2 and 4/1 (Table 2). A Bruker Vertex 70 Fourier transform spectrometer is utilized to get the VNIR reflectance spectra of these samples. For each sample, four reflectance spectra are measured with
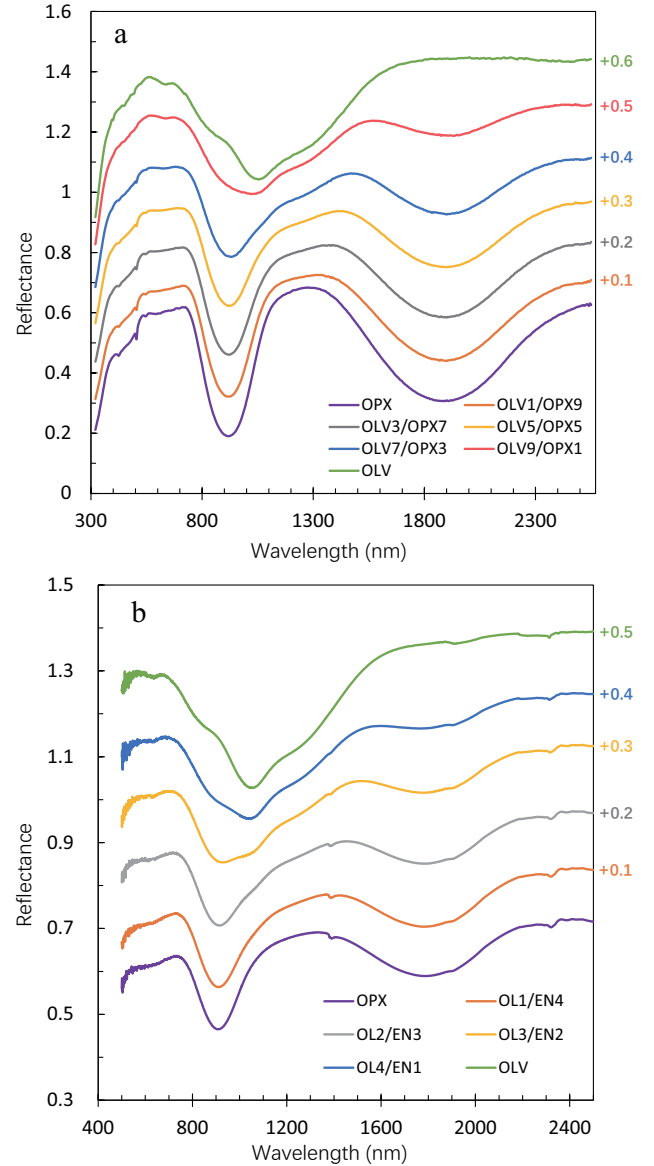

Fig. 3 VNIR reflectance spectra of mixtures composed of olivine and orthopyroxene mixed with different proportions. (a). The spectra are obtained from the RELAB database. (b). Spectral profiles are taken from our experiments (2.14 μm artificial peaks are removed, narrow ∼1.41 and ∼2.33 μm absorption bands presented in some spectra are due to minor alteration). Intuitively, the magnitude of reflection spectra gradually increases in the proportion of 0.1 as the abundance of olivine increases.

the different holder positions evenly distributed on the plane with a gap of 90°. Then their mean spectrum is taken as the final spectrum to reduce the effect of any surface inhomogeneity (Jiang et al. 2019). What needs our attention here is that the VNIR reflectance spectra of these materials have an artificial peak near 2.14 μm when a Spectralon panel made of polytetrafluoroethylene is placed as the calibration plate in the near-infrared
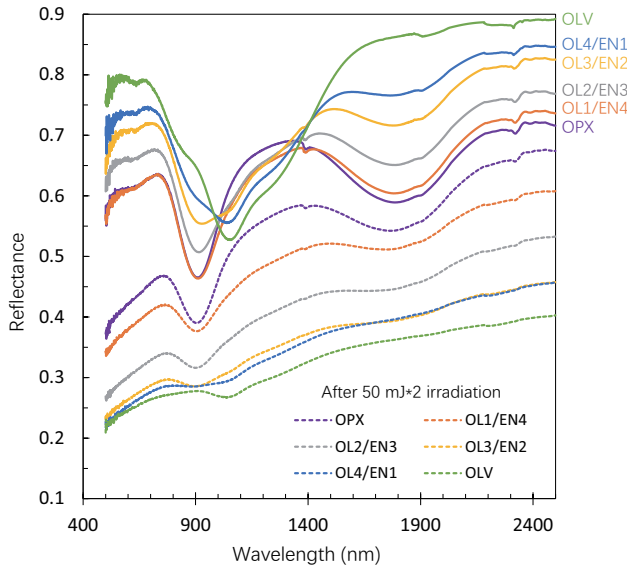
Fig. 4 VNIR reflectance spectra of mixtures composed of olivine and orthopyroxene mixed with different proportions before (*solid lines*) and after (*dashed lines*) 50 mJ*2 laser irradiation. Narrow ~1.41 and ~2.33 μm absorption bands present in some spectra are due to minor alteration. The colors of spectral curves are the same as in Fig. 3(b).
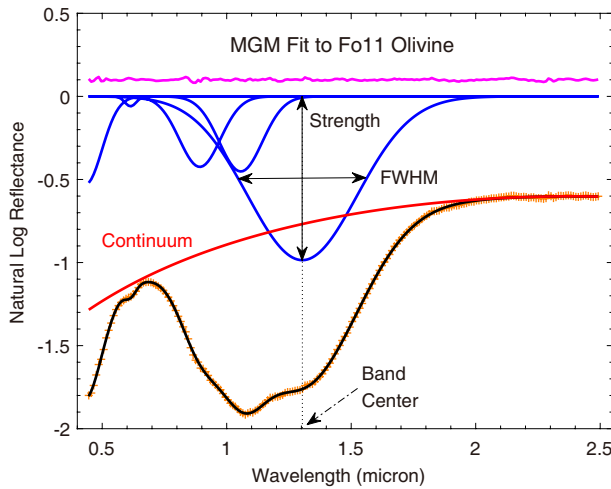

Fig. 5 Four significant characteristic parameters for MGM fitting. For the sake of clarity, the residuals (*pink line*) are shifted by +0.1 on the ordinate.

(NIR) region (Zhang et al. 2014). Two narrow spectral faint wobbles near 1.41 and 2.33 μm absorption bands present in some spectra are due to minor alteration. These two small fluctuations do not affect the results of this study, because these artificial wobbles are not on the main band absorption regions (Fig. 3(b)). However, we do need to remove the 2.14 μm artificial peak, as it appears in the orthopyroxene absorption features. Here, we utilize a 4th-order polynomial to fit the data between 1.8 and 2.5 μm.

Then the data of the artificial peak (~2.03 to ~2.18 μm) are replaced for further study. The modified reflectance spectra are featured in Figure 3(b).

2.2 Pulsed Laser Irradiation

The detailed experiment process can be found in Jiang et al. (2019). Here is a brief summary: In order to study the space weathering effects on olivine, orthopyroxene and their mixture spectra, some natural pure olivine and orthopyroxene powders (less than 75 μm) are mixed with certain fractions. Each time, ~1.0 g of powder samples is uniformly placed in a 2.5 cm × 2.5 cm square in an aluminum holder. These powder samples are baked in a dry oven at 120°C for about 12 hours to remove moisture. The dried samples, covered by a thin glass slide to prevent the powders sputtering, are placed in a vacuum chamber to cool to room temperature and then subjected to pulsed laser irradiation at a pressure of 10^{-3} Pa.

A nanosecond pulsed laser ($1 \sim 50$ mJ incident energy per pulse) is utilized as a micrometeorite bombardment simulation system with pulse frequency of 15 Hz. The laser spot is focused to a circle with a diameter of 0.5 mm using a lens and its moving speed is 1 mm s^{-1}. Researches indicate that after low-energy laser irradiation, the reflectance of olivine has a much greater change than that of pyroxene. Even after multiple irradiations, the depth of the pyroxene absorption band does not change much (Yamada et al. 1999; Jiang et al. 2019). In order to better simulate space weathering, we choose the maximum energy density (50 mJ) to irradiate the powder samples twice. The first irradiation is to translate in the vertical direction, and the second time is to translate in the horizontal direction. Each irradiated sample is measured immediately after irradiation. Original and irradiated reflectance spectra with the 2.14 μm artificial peak removed are displayed in Figure 4.

The irradiation energy density is set to be 3000 mJ mm^{-2} for each sample in our experiments. Due to the reflection and absorption of the glass, the energy transmission rate through the vacuum chamber glass window is about 90%. Considering energy loss as the presence of the glass lens, glass slide and aluminum sample holder, as well as the barrier effect caused by the npFe^{0} vapor deposition and the mineral particles adhering to the inner surface of the glass slide, we assume that 10% of the energy is absorbed by the samples, so the energy deposition is about 300 mJ mm^{-2}. Total energy deposition rate by dust impacts at 1 AU is estimated to be about 10^{-3} J m^{-2} yr^{-1} based on the calculations of Yamada et al. (1999) and Sasaki et al. (2001). Possibly,
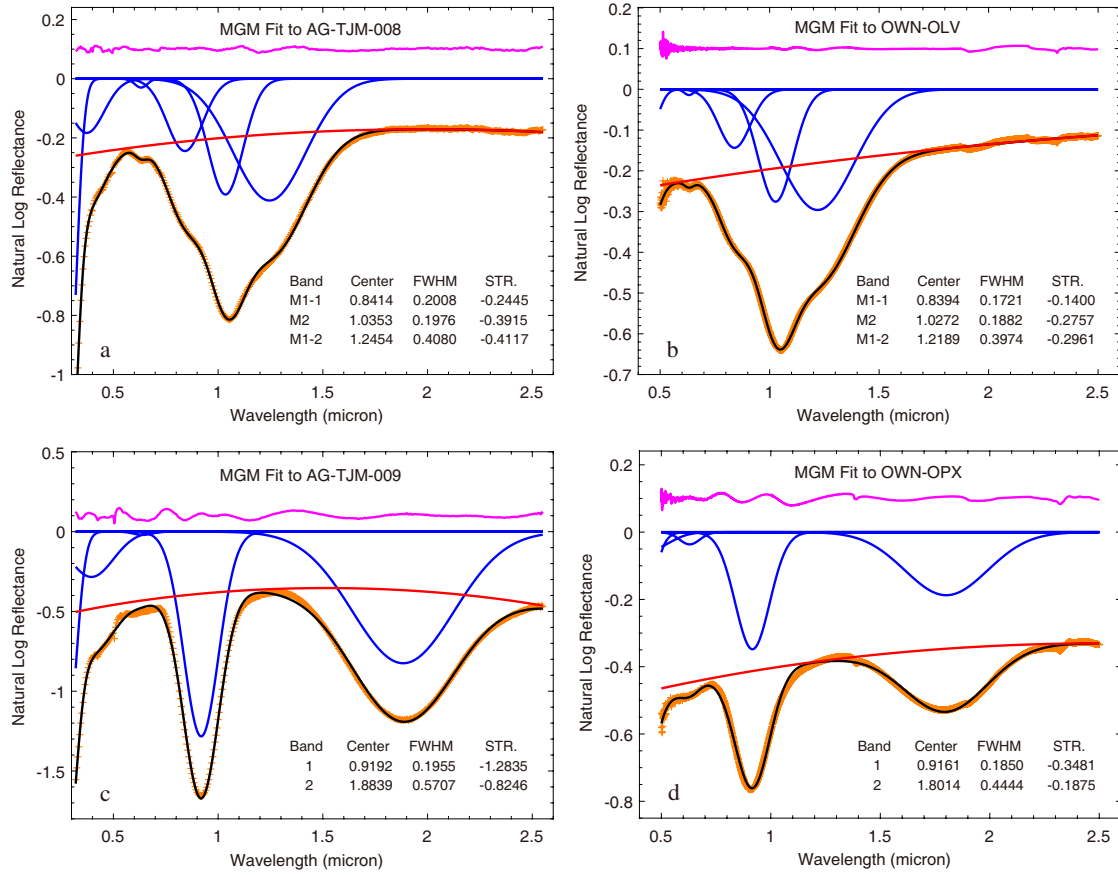
Fig. 6 The comparison of MGM fitting results for the spectral curves with olivine and orthopyroxene obtained from RELAB database (panel (a): RELAB olivine and panel (c): RELAB orthopyroxene) and our experiments (panel (b): OWN olivine and panel (d): OWN orthopyroxene).

the irradiation of samples in our experiments corresponds to about 300 Myr in space.

2.3 The Modified Gaussian Model (MGM)

Originally developed by Sunshine et al. (1990), modified Gaussian model (MGM) is a mathematical process based on the absorption of electronic transitions and is a statistical method for studying probability distribution. It is a mathematical procedure for deconvolving the superposed absorption features (Sunshine & Pieters 1993). The MGM program can be obtained from Brown University [2]. So far, some complex minerals and rock samples have been explored with the MGM approach (e.g., Noble et al. 2006; Clénet et al. 2011; Pinet et al. 2016). However, we need more efforts to improve our spectral modeling and interpretation capability when dealing with the spectra of natural unknown mafic bodies.

To elaborate on this model, four significant characteristics are used for interpreting and exploiting the MGM, which are: band center, full width at half maximum

(FWHM), band strength and continuum, as illustrated in Figure 5. In the MGM program, the natural logarithm of each spectral curve is modeled in energy domain (wave number), which means in wavelength domain a natural logarithm spectrum can be deconvolved into multiple Gaussian distributions with a continuum. MGM is modeled as

$$\ln\left[R\left(\lambda\right)\right] = C\left(\lambda\right) + \sum_{i=1}^{N} S_i \exp\left[-\frac{\left(\lambda^{-1} - \mu_i^{-1}\right)^2}{2\sigma_i^2}\right] \quad (1)$$

where λ is the wavelength, $R(\lambda)$ is the reflectance at wavelength λ, S is the band strength, μ is the band center, σ is the bandwidth and N is the number of bands. $C(\lambda)$ is a function of the continuum in wavelength space.

Here the continua are fitted by relying on the logarithm of a second-order polynomial. Continua are modeled close to the inflection regions of each absorption band, and we set an uncertainty within 20% for each parameter

$$C\left(\lambda\right) = \ln\left(c_0 + c_1\lambda + c_2\lambda^2\right) \quad (2)$$

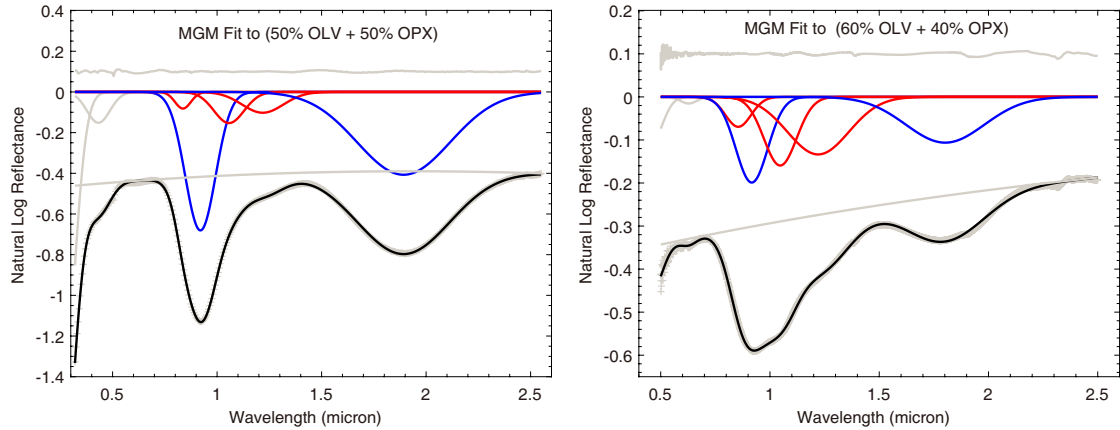λ = wavelength, c_0, c_1, c_2 = constants

Fig. 7 MGM fitting results for the samples composed of olivine and orthopyroxene mixed with different proportions. The fitting curves with the OPX absorption features are plotted as the blue curve. The red curve represents the olivine absorption band fitting by using the Gaussian function.

3 RESULTS AND DISCUSSIONS

3.1 MGM Parameters of Olivine and Orthopyroxene

In VNIR regions, olivine spectra display a broad and complex absorption feature near $1.0\,\mu m$. The Gaussian curves presented in the top panels of Figure 6 indicate that olivine spectra are composed of three individual absorption bands. They are around $0.84\,\mu m$, $1.03\,\mu m$ and $1.23\,\mu m$ respectively, which are assigned to the M1-1, M2 and M1-2 sites in the olivine crystal (Burns 1970). The width of each Gaussian absorption band in olivine spectra is related to the iron abundance in an olivine crystal and their ratio can be applied to constrain the parameters in MGM (Sunshine & Pieters 1998). Preliminary analyses of band strength derived by the MGM from olivine reflectance spectra affirm the bandwidths of M1-1 and M2 are similar but the width of M1-2 is about twice as large as M1-1 and M2. Analogously, the absorption strength can also be evaluated as a function of composition. Band strengths of M2 and M1-2 are similar and about twice that of M1-1.

3.2 MGM Parameters of Olivine-Orthopyroxene Mixtures

The initial MGM parameters of the olivine and orthopyroxene in the two end-member mixture can be regarded as constraints for further analysis of mixture spectra. We utilize these parameters to initialize the MGM and an intermediate ratio mixture in each group for spectral deconvolution. They are sample IDs: AG-TJM-019 (50% OLV + 50% OPX) in RELAB and OWN-OL3/EN2 (60% OLV + 40% OPX) in our experiment. The starting and final parameters of these two spectra in the MGM program are listed in Table 3 and the fitting results are depicted in Figure 7.
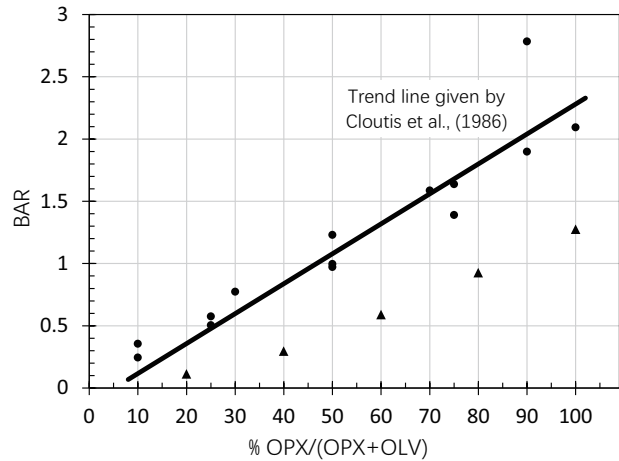

Fig. 8 BAR values derived from the spectra with olivine-orthopyroxene mixtures utilized in this study. The solid line represents the trend line given by Cloutis et al. (1986). Black dots and triangles signify the results estimated from RELAB and our original experiment samples respectively.

VNIR reflectance spectra of low-Fe orthopyroxene are dominated by the absorptions near $0.92\,\mu m$ and $1.85\,\mu m$ (bottom panels in Fig. 6). Each absorption is primarily caused by one electronic transition absorption band (Sunshine et al. 1990). The strength of the $\sim0.92\,\mu m$ band is stronger than that of the $\sim1.85\,\mu m$ band, whereas the bandwidth of $\sim1.85\,\mu m$ absorption is more than twice as large as the $\sim0.92\,\mu m$ absorption band.

The results indicate that when olivine and orthopyroxene are mixed in equal amounts, orthopyroxene dominates the spectral absorption features of the mixture. As displayed in Figure 6 and Figure 7, the center positions of the orthopyroxene's absorption bands are relatively stable, the strength is close to half of the pure orthopyroxene and the ratio of FWHM parameters remains the same.
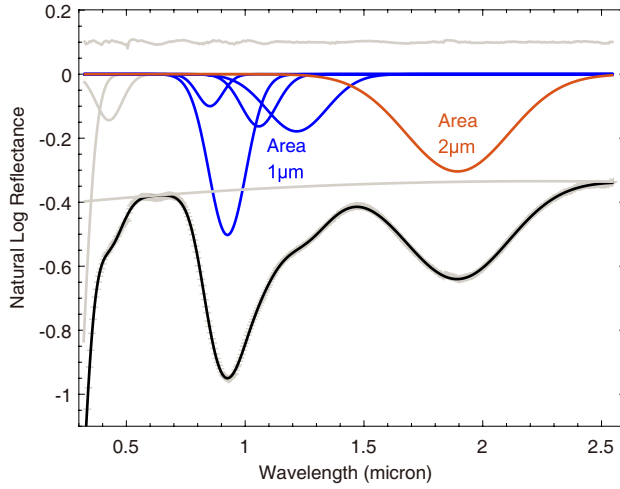
Fig. 9 The spectral diagnostic feature of MBAR derived from MGM fittings. For the obvious absorption feature close to 1.0 μm, the area of this band composed of four Gaussian curves (*signified as blue*) is defined as Area_1 μm. For the band at around 2.0 μm, this feature is made by a single Gaussian curve with orthopyroxene (*orange line*) and then defined as Area_2 μm.
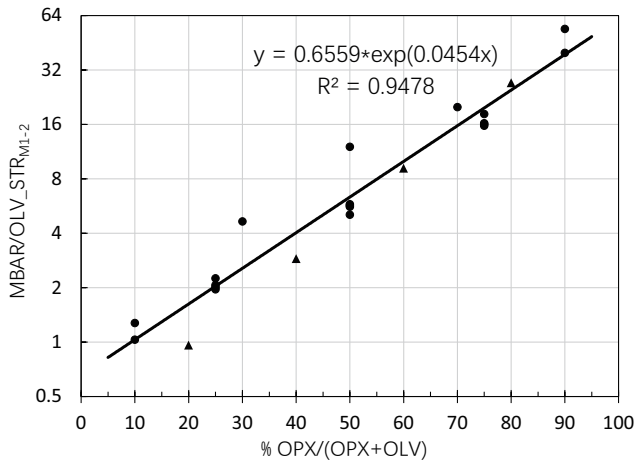

Fig. 10 A plot of MBAR/OLV_STR$_{M1-2}$ ratio versus orthopyroxene abundance. The solid line represents a linear least-squares fit for all data with the orthopyroxene abundance between 10% and 90%. The notations of data points are the same as Fig. 8.

However, parameters of the three Gaussian absorption bands in olivine spectra change a lot, the strength of each absorption band is about 1/3 that of the pure olivine mineral and the strongest absorption M1-2 band decreases sharply. When the content of olivine is more than orthopyroxene, the spectral curve of the mixture near the 1.0 μm region shows a broad asymmetric complex absorption feature, and the absorption features of olivine dominate the spectral curve between the 1.0 and 1.5 μm regions.

3.3 Modified BAR of Olivine-Orthoyroxene Mixtures

We also utilize the band area ratio (BAR) method (Cloutis et al. 1986) to analyze these spectra. The BAR method does not need MGM processing and it is generally considered as a very useful indicator for interpreting the olivine-orthopyroxene mixture spectra, which is nearly independent of mineral composition and mineral grain size (Cloutis et al. 1986). However, we found that the BAR values of each mixture sample group exhibit a clearly-defined linear trend, but not all of them follow the trend line given by Cloutis et al. (1986). In the calculation results of some samples, especially for the BAR values of our newly acquired spectral curves, the deviation between the estimated mineral abundance value and its true value may be more than 30% (Fig. 8).

The deviations are mainly caused by using different spectrometers, since band depths and band shapes depend on illumination and viewing geometry as stated in Hapke (2005). It can cause differences in band shapes between spectra of the same material measured bidirectionally and utilizing an integrating sphere to measure the directional-hemispherical reflectance. Therefore, we should regard this trend line with caution, especially when the spectrometers and/or the viewing geometry used for measurement are different and the abundances and/or end-member chemistries are unknown. Fortunately, the good linear trend displayed by each BAR parameter group provides a direction for solving this problem. As depicted in Figure 6 and Figure 7, M1-2 band (∼1.23 μm) in the olivine absorption features is able to be distinguished from the absorption band of orthopyroxene. The absorption strength of the olivine M1-2 band and overall absorption feature near 1.0 μm contain information about the relative content of olivine and orthopyroxene. It indicates that we can rely on the MGM fitting results to estimate the mineral abundance.

Firstly, we utilize MGM to obtain the absorption features of olivine and orthopyroxene in the mixtures. Secondly, a modified band area ratio (MBAR) indicator is obtained by using MGM fitting result parameters. The MBAR is modeled as

$$\mathrm{MBAR} = Area\_2\mu m / Area\_1\mu m \qquad (3)$$

where *Area* is calculated with an approximation and it is defined as

$$Area = \sum_{i=1}^{N} 1.065 * FWHM_i * STR_i . \qquad (4)$$

Here 1.065 is the factor to get the integral of Gaussian curve by using *FWHM*. *STR* is the absolute value of absorption strength. There are four absorption bands in
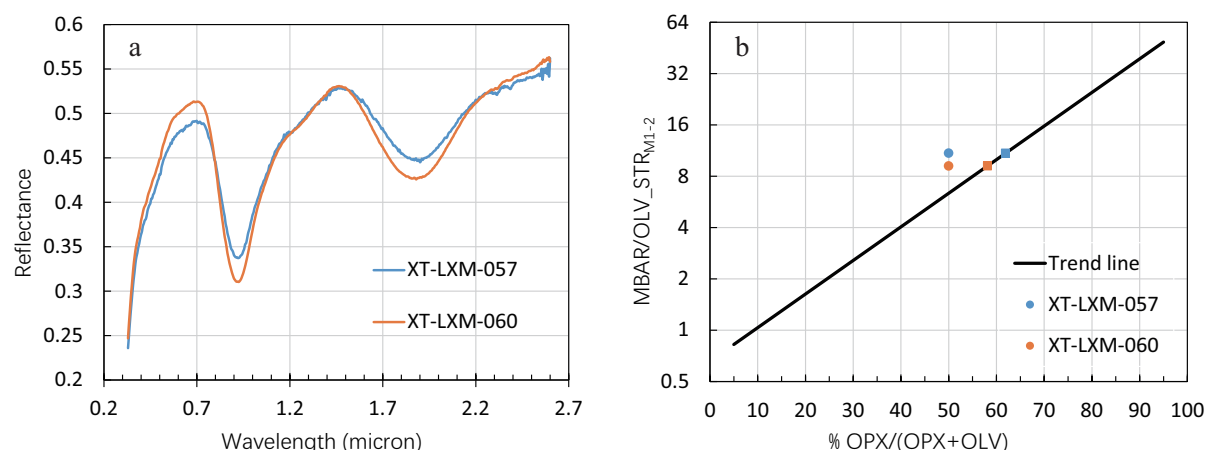
Fig. 11 Spectral reflectance of two RELAB olivine-orthopyroxene mixture samples and mineral abundance estimation results obtained by MGM. Dot represents the true value and square signifies the estimated value.

Area_1 μm, which are the three diagnostic absorption features of olivine and one absorption of orthopyroxene (that is Band 1). There is only one orthopyroxene absorption band (Band 2) in Area_2μm. The illustration in Figure 9 illustrates these definitions in detail.

Finally, MBAR can be regarded as the absorption intensity coefficient of the two main absorption bands in the olivine-orthopyroxene mixture spectra. As mentioned above, the M1-2 band in olivine spectra is easy to extract from the mixture spectral curves. Dividing MBAR by the olivine M1-2 band absorption strength value (abbreviated as: MBAR/OLV_STR$_{M1-2}$) can get the end-member composition information. The resulting values show a good pattern on the estimation results, as the orthopyroxene abundance increases, the MBAR value increases, the OLV_STR$_{M1-2}$ value decreases and the ratio data of the two values manifest an exponential growth trend. In order to visualize their changing patterns clearly, we use an exponential ordinate to display them. Figure 10 features the calculation results and the regression equation. The overall error in predicting the mixture composition based on MGM fitting results is less than 15%.

Here, to test the deconvolution analysis and the trend lines described above, we choose two olivine-orthopyroxene mixture samples with the same end-member minerals as examples (RELAB ID: XT-LXM-057 and XT-LXM-060, whose grain sizes are $32 \sim 63$ μm, with 50% olivine + 50% orthopyroxene). These two reflectance spectra are measured by placing identical samples in different sample dishes. XT-LXM-057 is placed in an aluminum dish coated with black Teflon and XT-LXM-060 is placed in a Nicolet dish. Two different spectral curves are obtained by changing the sample holding dishes. Their reflectance spectra are plotted in Figure 11(a). The deconvolution fitting results are obtained by applying the MGM and the mineral abundance estimation results

are depicted in Figure 11(b). MBAR values of the two mixture samples are 0.850 and 0.861, and olivine M1-2 band absorption intensity values are $\sim$0.078 and $\sim$0.094. MBAR/OLV_STR$_{M1-2}$ values are 10.9 and 9.2 respectively. The orthopyroxene abundance estimation results are 61.9% and 58.1%. Compared to the true value (50%), these two results are all within the accuracy range of 15% given above.

3.4 Fitting Results of Irradiated Samples

Some RELAB samples irradiated with the pulsed laser to simulate the effect of space weathering are mentioned in Table 2, but it seems no significant spectral alteration appears in their spectral curves. However, for our samples, the fresh spectra and spectra irradiated by a high energy laser show obvious differences (Fig. 12), which are suitable for further study. After irradiation, the spectral features turn weaker and shallower. Absorption intensity and albedo of the visible region decrease faster than in the NIR region, whose behaviors redden and darken the irradiated VNIR spectra. In a high-intensity or long-term space weathering environment, the spectra of pyroxene appear more reddened, and olivine spectra appear more darkened. This is consistent with the results presented in Yamada et al. (1999) and Jiang et al. (2019).

A widely utilized continuum removal method is employed to compare the spectral absorption features and the band depth of these samples before and after pulsed laser radiation (Clark & Roush 1984). Band center positions of the continuum-removed spectra before and after laser irradiation are compared in Table 4. It is generally believed that continuum-removed band positions are less affected (shifted by a few nanometers) by space weathering (Pieters et al. 2000; Fu et al. 2012). Figure 13 features the parameter comparison of these original and
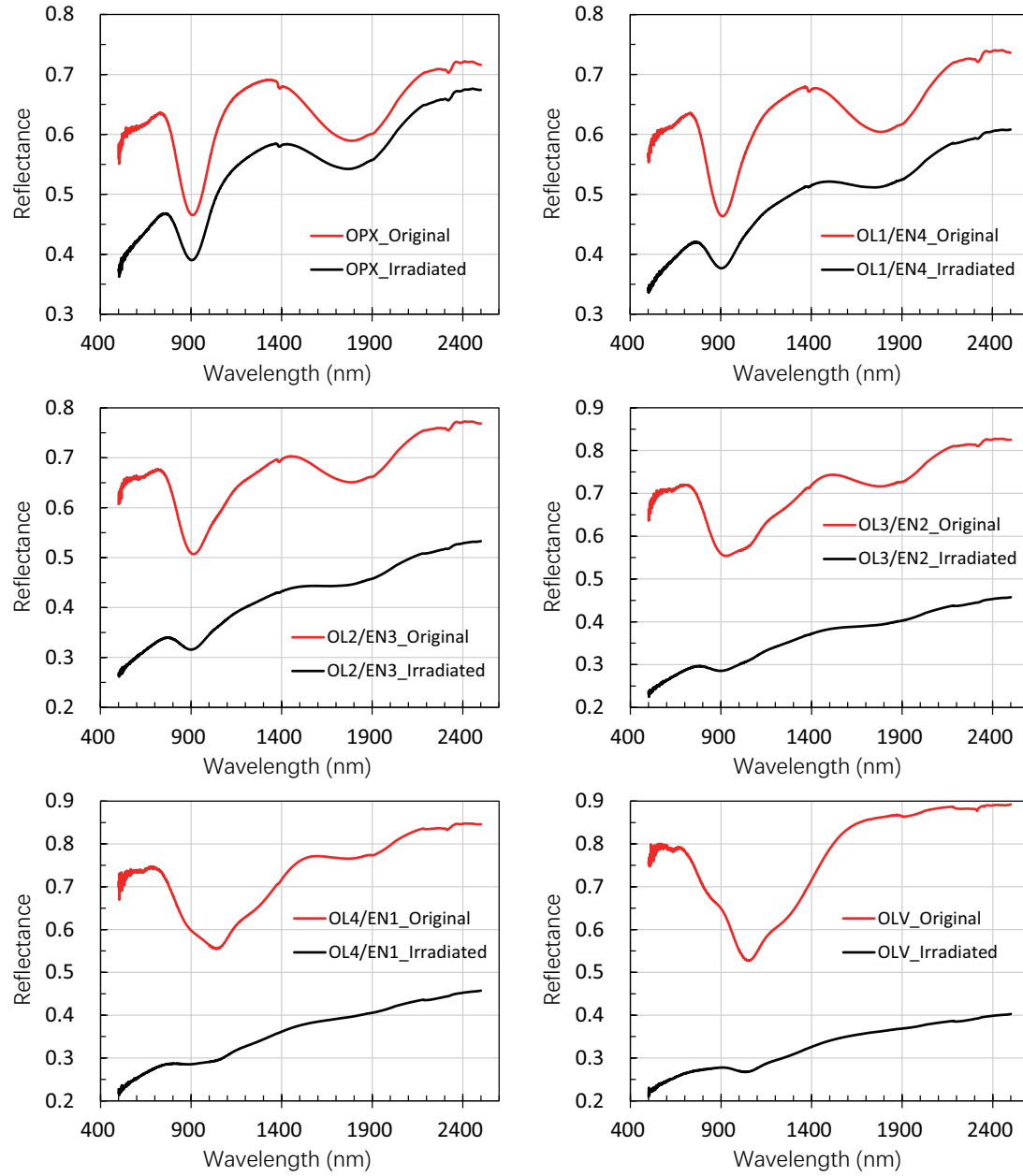
Fig. 12 Comparison of the spectral curves composed of olivine-orthopyroxene admixtures mixed with different proportions and their irradiated results.

irradiated spectral curves. The absorption features near 1.0 μm are the superposition of olivine and orthopyroxene. Obviously, the higher the proportion of olivine is, the more band depth decreases after laser irradiation. While the absorption features near 2.0 μm are only due to the spectral absorption of orthopyroxene, the spectral curves in this region change uniformly. A sub-figure shows the albedo value of these samples and here it uses the average of the spectral reflectance from 0.5 to 0.8 μm (close to the visible region). This figure affirms that orthopyroxene has stronger resistance to space weathering than olivine. On the whole, the higher the content of olivine in the mixture is, the

weaker absorption features are in its irradiated spectra, which may make these spectra more difficult to identify and interpret.

Also, we deconvolve these space weathered spectra based on the prior mineral knowledge and the constraints mentioned above. After pulsed laser irradiation, the MBAR of these samples all increase (Fig. 14(a)). It can be inferred that the spectra at the short wavelengths are more susceptible to space weathering than those at the longer wavelengths in the VNIR region. What is more, as olivine is more susceptible to space weathering, the spectral absorption strength of olivine will reduce significantly.
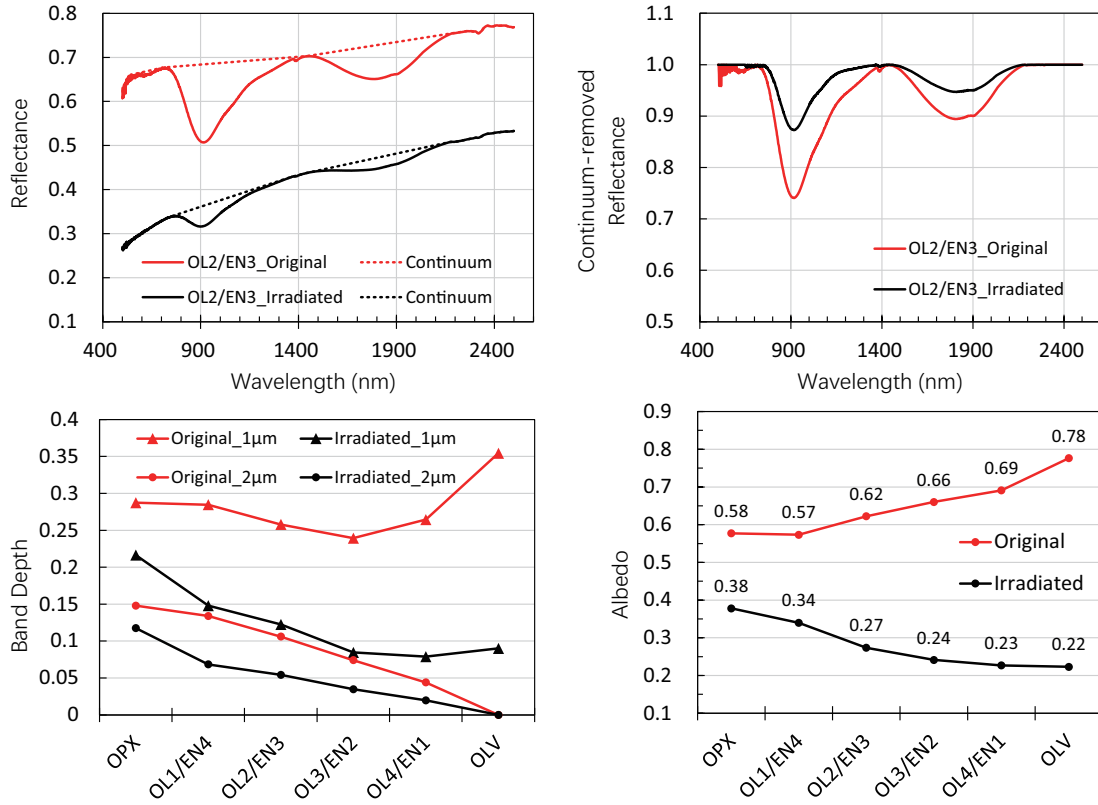
Fig. 13 Variations of band-depths and albedos (average of the spectral reflectance ranging from 0.5 to 0.8 μm) of olivine-orthopyroxene mixtures before and after pulsed-laser irradiation.
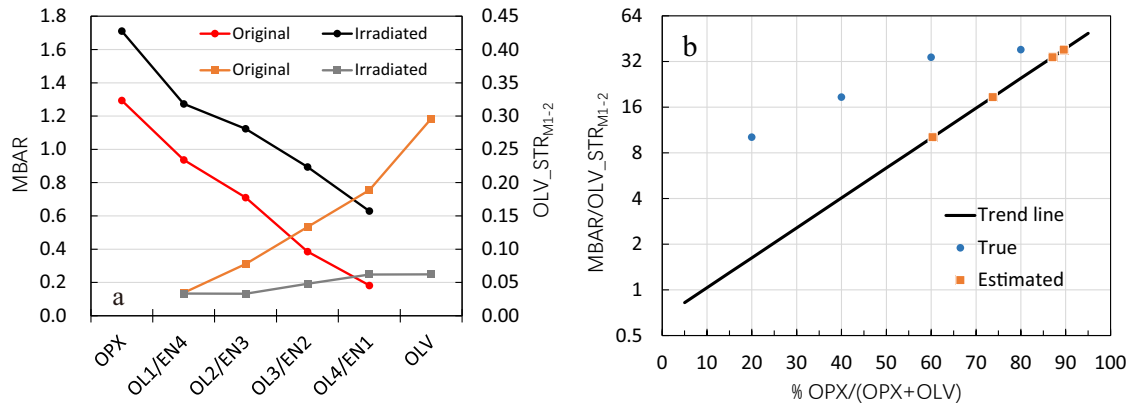

Fig. 14 Deconvolution results of the olivine-orthopyroxene mixtures derived from MGM fittings. (a). The evolution of MBAR ratios (Band M1-2 absorption strengths) of olivine-orthopyroxene mixtures with different proportions before and after pulsed-laser irradiation. (b). Correlation of true and estimated abundances of the mixtures with pulsed-laser irradiation, where the blue circles and orange squares represent the true and estimated abundances of these mixtures respectively.

The more olivine content is in the mixtures, the greater the ratio decrease of Band M1-2 absorption strength (Fig. 14(a)), which will further increase the deviation in the mixture composition prediction results. MGM deconvolution results of these irradiated mixtures are displayed in Figure 14(b). The distance between two points in the horizontal direction represents the deviation value of

the prediction result. With the increase of olivine (decrease of orthopyroxene) content, the deviation of estimated results also increases.

In addition, an extended calculation shows that it will get a slightly larger MBAR/OLV_STR$_{M1-2}$ value than the original spectrum when using MGM to deconvolve the continuum-removed spectrum, which means it will slightly
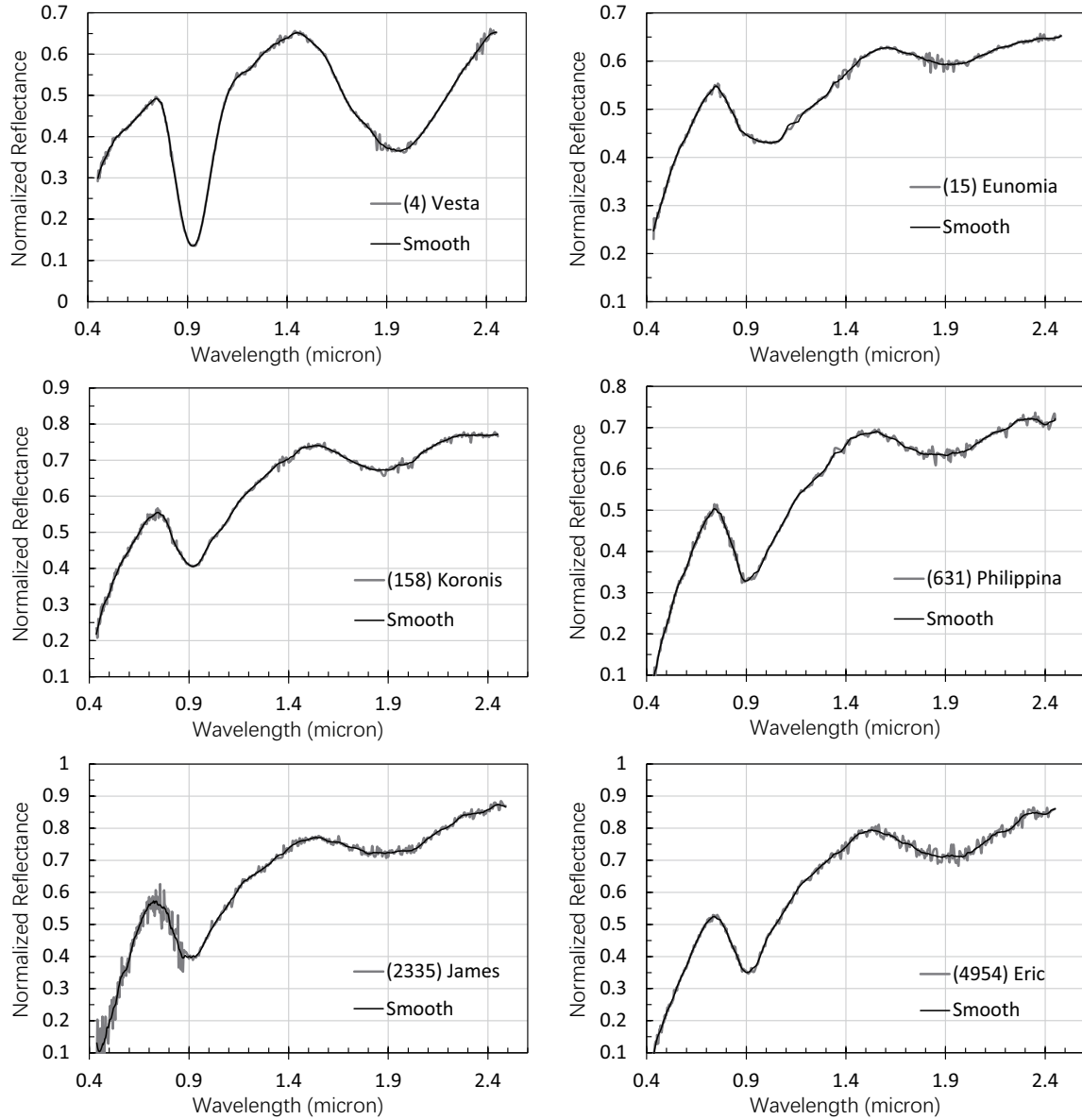
Fig. 15 VNIR spectra of six asteroids: (4) Vesta, (15) Eunomia, (158) Koronis, (631) Philippina, (2335) James and (4954) Eric. These spectra are normalized at 0.55 μm and shifted downward to suitable positions.

underestimate the olivine abundance. This finding will be considered later. All these results remind us that we cannot be too cautious when identifying and interpreting the spectra of space weathered celestial bodies. If the effect of space weathering is not taken into account, MGM deconvolution results will usually underestimate the proportion of olivine in the mixtures.

3.5 Estimating the Composition of Olivine-Orthopyroxene Asteroids

The research results obtained above are very promising and they can be applied to study space weathered celestial bodies, such as asteroids or lunar rocks. Asteroids are

considered to be smaller and rotating faster than solid planets, with minimal gravity, and these asteroids have thinner regolith (Chapman 2004). Q-type and S-type asteroids are characterized by spectra with moderate silicate absorption features near 1.0 and 2.0 μm (Chapman 2004; DeMeo et al. 2015). Vernazza et al. (2008) and Thomas et al. (2014) analyzed the VNIR spectra of many Q-type and S-type asteroids and reported that most of them have spectral properties similar to LL chondrites, whose main minerals are hypersthene and olivine. Here we choose some asteroids dominated by olivine-orthopyroxene for further study to estimate their mineral compositions.
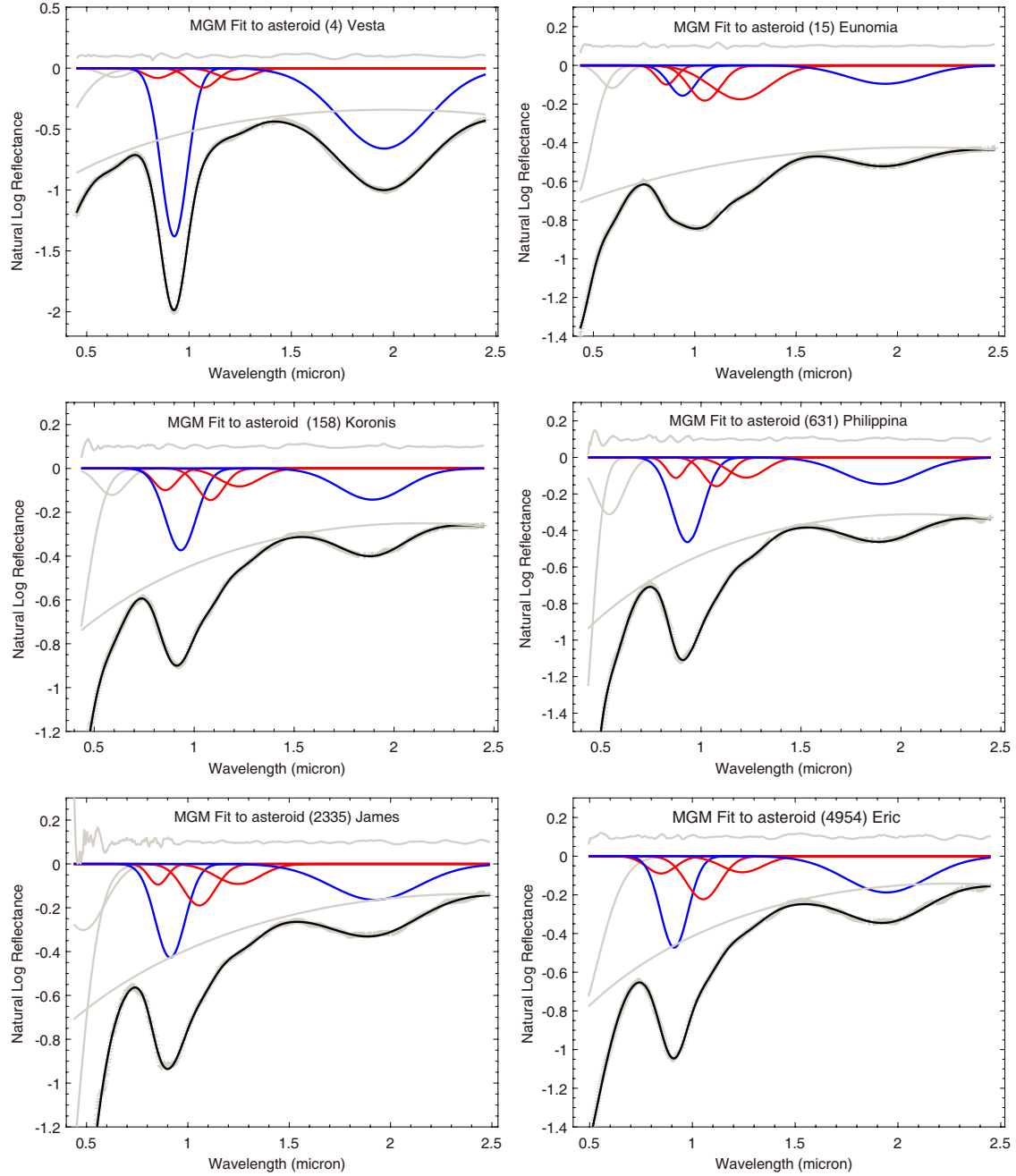
Fig. 16 Decomposition of the components of 1.0 and 2.0 µm features for six asteroids (4) Vesta, (15) Eunomia, (158) Koronis, (631) Philippina, (2335) James and (4954) Eric. The OPX absorption bands fitted by MGM method are plotted as blue curves and red lines represent the absorption features with olivine. The black curves are the sum of all band profiles plus the continuum.

Table 5 MGM Results and Mineral Abundance Estimation Results of the Asteroids

Asteroids	Area_1µm	Area_2µm	OLV_STR$_{M1-2}$	Calculation	OLV : OPX
(4) Vesta	264.48	341.82	0.0939	13.76	33% : 67%
(15) Eunomia	127.96	41.89	0.1752	1.87	77% : 23%
(158) Koronis	123.33	55.31	0.0821	5.46	53% : 47%
(631) Philippina	144.59	63.87	0.1103	4.00	60% : 40%
(2335) James	142.63	83.67	0.0915	6.41	50% : 50%
(4954) Eric	152.56	88.34	0.0832	6.96	48% : 52%

Calculation represents the value of MBAR/OLV_STR$_{M1-2}$.
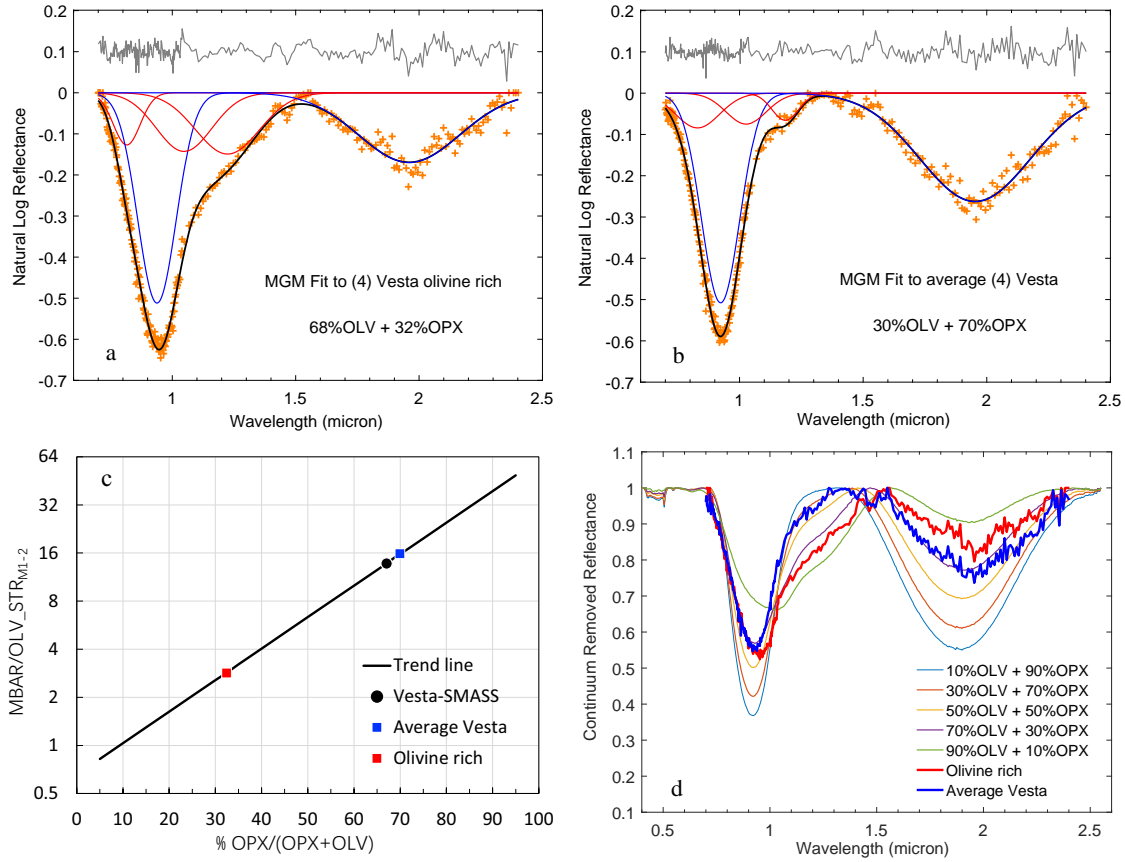
Fig. 17 Decomposition of the components of absorption features for main-belt asteroid (4) Vesta. (a). Modeled spectral fitting of the crater area that is olivine-rich. (b). Modeled spectral fitting of average Vesta spectrum. (c). The estimations of mineral abundances derived from the SMASS and Dawn spectral data. (d). Comparison of the continuum-removed spectra obtained from various areas on (4) Vesta. (Data from Ammannito et al. (2013) and olivine-orthopyroxene systematic mixtures have different proportions.)

3.5.1 *Spectral Deconvolution on Olivine-Orthopyroxene Asteroids*

The center positions of the $2.0\,\mu m$ absorption band are useful for determining the compositions of pyroxene. Low-Fe orthopyroxene spectra confirm that the absorption band center near $2.0\,\mu m$ is ranging from 1.80 to $1.95\,\mu m$ (Klima et al. 2007). Such information can help us to search for suitable asteroid spectra for studying their mineralogical characterization. Six asteroids with high quality spectra are selected, they are: (4) Vesta, (15) Eunomia, (158) Koronis, (631) Philippina, (2335) James and (4954) Eric. The VNIR spectra of these asteroids are obtained from the Small Main-Belt Asteroid Spectroscopic Survey (SMASS), which are presented on the MIT planetary spectroscopy website [3].

Absolute spectral albedos are difficult to obtain with accuracy in many remote sensing situations, so all spectra from MIT are normalized to unity at $0.55\,\mu m$. This work smoothed and shifted these asteroid spectral

reflectance curves to acclimatize to the MGM. First, the spectra are smoothed utilizing the Savitzky-Golay (SG) filter procedure (order = 3 and framelen = 25) (Savitzky & Golay 1964). Then, the spectral curves should be shifted to suitable positions: if the maximum value of the asteroid albedo is less than 1.4, the whole spectral curve will be shifted downward by 0.6, while if it is greater than 1.4, it will be shifted downward by 0.7 (Fig. 15). The purpose of this shifting operation is to ensure that the spectral curves of these silicate-rich asteroids can be compared with the experimental spectra. Subject to slight space weathering, the slope of the mafic mineral spectra will increase slightly. The steep visible band region and overall inclined spectral curves reveal that these asteroids have suffered space weathering.

It is feasible to use the MGM deconvolution approach to estimate the mineral abundances. MGM with the logarithm of a second-order polynomial continuum removal method is employed to deconvolve these spectra. The deconvolution and estimated results are displayed in Figure 16 and Table 5. As shown in Figure 14 and
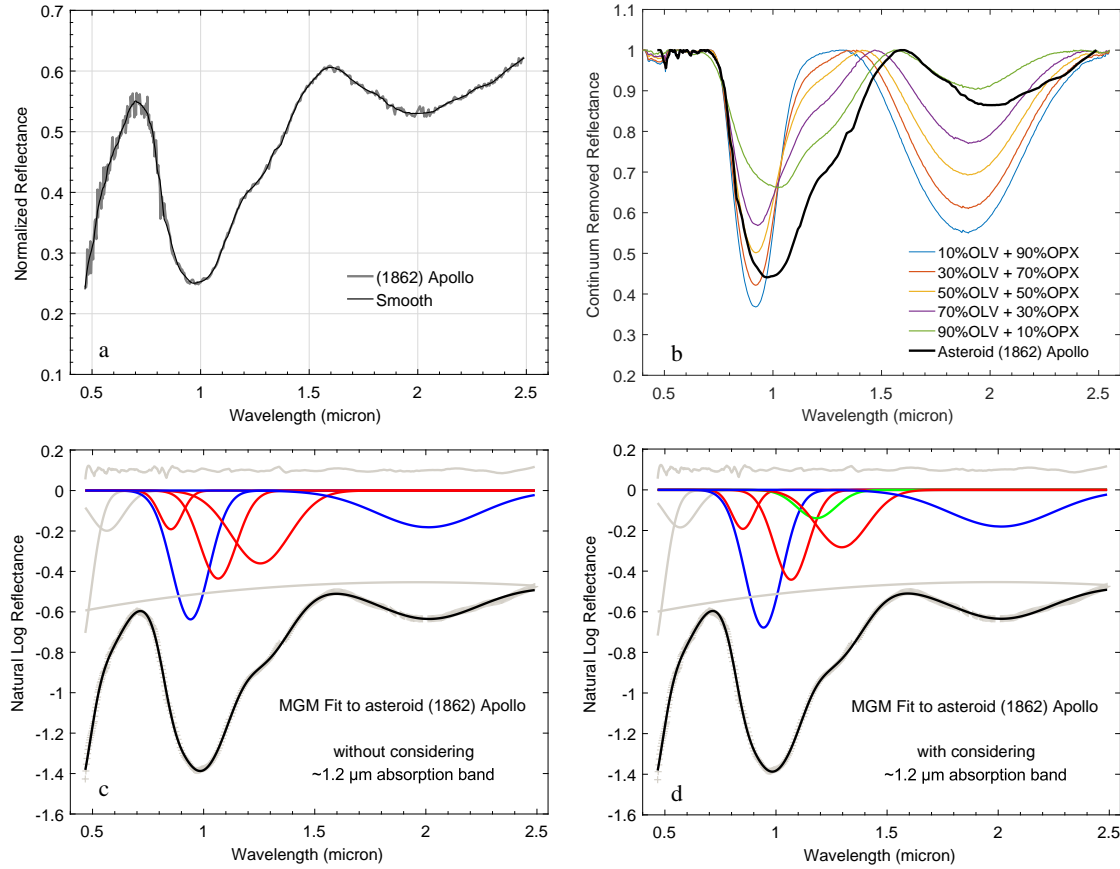
---

[3] *http://smass.mit.edu/home.html*

Fig. 18 VIR spectral curve of asteroid (1862) Apollo and decomposition of the components of 1.0 and 2.0 μm features. (a). The observed and smoothed spectra are normalized at 0.55 μm and shifted downward to suitable positions. (b). Comparison of the continuum-removed spectral curves and olivine-orthopyroxene mixtures with different proportions. (c). Decomposition of the components of absorption features without considering ∼1.2 μm sub-band composed of high-Fe orthopyroxene. (d). The curve is fitted by following the same method as in panel (c), but considering the ∼1.2 μm absorption band (*marked as a green line*).

described above, MGM will usually underestimate the proportion of olivine in the mixtures when deconvolution is applied to space weathered spectra, so the olivine content on these asteroids is only conservatively estimated in this paper. It means that the fresh rocks or subsurface materials of these asteroids may contain more olivine.

3.5.2 More Olivine on Asteroid (4) Vesta

Asteroid (4) Vesta is the second most massive and probably the second largest asteroid (Thomas et al. 2005). It has been considered that olivine and hypersthene are likely to be ubiquitous over the whole surface of Vesta (e.g., Donaldson Hanna & Sprague 2009; Ammannito et al. 2013; Zambon et al. 2014; Le Corre et al. 2015; Poulet et al. 2015). Ammannito et al. (2013) analyzed the average spectra of (4) Vesta and indicated an olivine-rich site from a bright crater. The spectrum of the bright crater reveals clear olivine signatures, with the band near 1.0 μm centered at a slightly longer wavelength than the

average (4) Vesta spectrum, and the area of the 2.0 μm band is smaller than the average spectrum. The data are plotted in Figure 17(d).

These data can be used to infer that the surface of the asteroid (4) Vesta contains a high content of olivine. The olivine modeled abundance is about 20%, and the spectra of some fresh rocks from the impact crater are interpreted as having an olivine content of more than 50%, maybe even up to 70% ∼ 80% (Ammannito et al. 2013; Clenet et al. 2014; Poulet et al. 2015). In order to deconvolve these two continuum removed spectral data, we adjusted the MGM parameters to the study in this work. The deconvolution results (depicted in Fig. 17) of the spectral data obtained by SMASS and Dawn are very consistent. Remote sensing and orbital average spectral data of the asteroid (4) Vesta affirm that there are about 30% olivine + 70% orthopyroxene in its surface mafic materials. However, the deconvolution results of the bright crater spectrum reveals that there is approximately 70% olivine. Considering that the spectrum of the bright impact

crater is continuum removed (as described at the end of Sect. 3.4) and it has also been slightly weathered in space, we infer that the olivine composition of partial craters on asteroid (4) Vesta is greater than 70%. This result is consistent with the findings of Ammannito et al. (2013) and Poulet et al. (2015). Based on these findings, we can infer that the other asteroids mentioned above also have a high olivine content. However, space weathering prevents the correct deconvolution and interpretation of these spectra.

3.6 Different Orthopyroxenes

The orthopyroxene measured in RELAB and our experiment are both low-Fe orthopyroxenes. To understand whether the mixture of olivine and high-Fe orthopyroxene is also suitable for the method presented here, we carried out the following study. As is shown in Figure 1(b), the spectral curve of ferrosillite, a kind of high-Fe orthopyroxene, manifests an obvious absorption characteristic near 1.2 µm. This spin-allowed crystal field absorption band is attributed to the presence of Fe^{2+} in the crystal M1 site, which is on the shoulder of the 1.0 µm band (Klima et al. 2007). This position is very close to olivine's M1-2 band and thus care must be taken when interpreting the data. In addition, the two main absorption bands centered around 1.0 and 2.0 µm shift towards longer wavelength as the iron content increases. Here we choose the asteroid (1862) Apollo (Fig. 18(a)) for further study, as its spectral curves feature an olivine reflectance peak near 1.6 µm with two high-Fe orthopyroxene absorption bands (Gaffey et al. 1989; Buratti et al. 2004).

The spectral curve matching method is used for this spectrum, and three absorption features near 1.0 µm, 1.2 µm and 2.0 µm are compared with systematic mixtures (Fig. 18(b)). The derived olivine abundance is about 80% in the olivine-orthopyroxene mixtures. Two MGM deconvolution procedures are utilized here, one considers the ∼1.2 µm absorption of the high-Fe orthopyroxene and the other does not consider this band. The deconvolution results are shown in Figure 18(c) and 18(d).

If we ignore the absorption of the ∼1.2 µm band, the deconvolution result of MGM will get a larger absorption intensity in the olivine M1-2 band than the one that adds the ∼1.2 µm absorption band. The actual ∼1.2 µm absorption band will increase the area of the 1.0 µm band, which will lead to the MBAR value decreasing. The combination of these two factors will be misinterpreted as the content of olivine in the material is higher than the actual abundance. Figure 18(c) affirms that the surface material of asteroid (1862) Apollo is composed of 96% olivine and 4% orthopyroxene, which does not meet our

expectation. However, Figure 18(d) shows it contains about 88% olivine and 12% orthopyroxene (here we have deducted the area of the ∼1.2 µm absorption band). Although the results of these two estimated values are close, we have demonstrated that the deconvolution result considering the ∼1.2 µm absorption band is relatively reliable.

4 CONCLUSIONS

In this article, a new empirical procedure based on MGM with some prior mineral absorption bands is presented to estimate the end-member abundance from olivine-orthopyroxene mixture spectra. The accuracy of the end-member abundance can be estimated within 15% by using this new procedure.

Integrated with the RELAB database, a new spectral set obtained from olivine-orthopyroxene mixtures assembled at 20% mineral abundance intervals in our experiments is exploited. The VNIR absorption spectra of olivine-orthopyroxene mixtures systematically varied with their various abundances. However, we found the commonly-used BAR does not work well for some mixtures and the BAR of different mixture sets show large deviations. As a powerful tool, MGM is utilized to reveal the composition of mafic mineral assemblages. An MBAR is introduced to describe a newly-defined BAR based on the fitted parameters by MGM. Two parameters of MBAR and olivine M1-2 band absorption strength (as defined in the MGM) are utilized to estimate the mineral abundances of olivine-orthopyroxene mixtures. The systematic procedure is quite efficient for deconvolution of olivine-orthopyroxene mixture spectra and estimation of the mineral abundances for mafic materials from the VNIR reflectance spectra.

Additionally, the effect of space weathering on olivine-orthopyroxene mixtures and silicate asteroids is investigated based on the newly proposed procedure. Some samples are irradiated by a high-energy laser in our experiments and the spectral profiles of these samples vary with irradiation fluxes significantly. After irradiation, we find that mineral diagnostic spectral features (∼1.0 and ∼2.0 µm bands) become weaker and shallower. The intensities of absorption bands and albedos of these spectra in the visible region decrease faster than those in the NIR region. The MGM deconvolution results of these irradiated mixtures indicate that orthopyroxene has stronger resistance to space weathering than olivine. Among the results, MBAR increases, while olivine M1-2 band absorption strength decreases, which makes these irradiated spectra more difficult to identify and interpret. This usually leads to an underestimate of olivine abundance. The VNIR spectra of main-belt asteroid (4)

Vesta from the SMASS catalog and Dawn mission are investigated by applying the new procedure and the results are consistent with other studies.

Besides, the influence of absorption band strength of high-Fe orthopyroxene at $\sim$1.2 μm is also discussed in this study and we claim that this band should not be ignored in the analysis of olivine and high-Fe orthopyroxene mixtures. In the future, more experiments on spectral deconvolution of different mafic mixtures and studies of various space weathering effects will be implemented to extend the applications of the newly proposed procedure and MGM.

References

Adams, J. B. 1974, J. Geophys. Res., 79, 4829

Ammannito, E., de Sanctis, M. C., Palomba, E., et al. 2013, Nature, 504, 122

Basilevsky, A. T., Shalygin, E. V., Titov, D. V., et al. 2012, Icarus, 217, 434

Bishop, J. L., Pieters, C. M., Hiroi, T., & Mustard, J. F. 1998, Meteoritics and Planetary Science, 33, 699

Brunetto, R., Romano, F., Blanco, A., et al. 2006, Icarus, 180, 546

Buratti, B. J., Britt, D. T., Soderblom, L. A., et al. 2004, Icarus, 167, 129

Burbine, T. H., McCoy, T. J., Nittler, L. R., et al. 2002, Meteoritics and Planetary Science, 37, 1233

Burns, R. G. 1970, American Mineralogist, 55, 1608

Chapman, C. R. 2004, Annual Review of Earth and Planetary Sciences, 32, 539

Clark, R. N., & Roush, T. L. 1984, J. Geophys. Res., 89, 6329

Clark, R. N., Swayze, G. A., Livo, K. E., et al. 2003, Journal of Geophysical Research (Planets), 108, 5131

Clenet, H., Jutzi, M., Barrat, J.-A., et al. 2014, Nature, 511, 303

Clénet, H., Pinet, P., Daydou, Y., et al. 2011, Icarus, 213, 404

Cloutis, E. A., Gaffey, M. J., Jackowski, T. L., & Reed, K. L. 1986, J. Geophys. Res., 91, 11641

Cloutis, E. A., & Gaffey, M. J. 1991, J. Geophys. Res., 96, 22809

Cloutis, E. A. 1996, International Journal of Remote Sensing, 17, 2215

Cloutis, E. A., & Bell, J. F. 2000, J. Geophys. Res., 105, 7053

Cloutis, E. A., Craig, M. A., Kruzelecky, R. V., et al. 2008, Icarus, 195, 140

Danyushevsky, L. V., Della-Pasqua, F. N., & Sokolov, S. 2000, Contributions to Mineralogy and Petrology, 138, 68

DeMeo, F. E., Alexander, C. M. O., Walsh, K. J., Chapman, C. R., & Binzel, R. P. 2015, The Compositional Structure of the Asteroid Belt, Asteroids IV (University of Arizona Press), 13

Donaldson Hanna, K., & Sprague, A. L. 2009, Meteoritics and Planetary Science, 44, 1755

Dyar, M. D., Sklute, E. C., Menzies, O. N., et al. 2009, American Mineralogist, 94, 883

Dybwad, J. P. 1971, J. Geophys. Res., 76, 4023

Elardo, S. M., Draper, D. S., & Shearer, Charles K., J. 2011, Geochim. Cosmochim. Acta, 75, 3024

Elkins-Tanton, L. T., Hess, P. C., & Parmentier, E. M. 2005, Journal of Geophysical Research (Planets), 110, E12S01

Elthon, D. 1979, Nature, 278, 514

Fu, X., Zou, Y., Zheng, Y., & Ouyang, Z. 2012, Icarus, 219, 630

Gaffey, M. J., Bell, J. F., & Cruikshank, D. P. 1989, in Asteroids II, ed. R. P. Binzel, T. Gehrels, & M. S. Matthews, 98

Gallie, E. A., Lyder, D. A., Rivard, B., & Cloutis, E. A. 2008, International Journal of Remote Sensing, 29, 4089

Garcia, M. O., Hulsebosch, T. P., & Rhodes, J. M. 1995, Washington DC American Geophysical Union Geophysical Monograph Series, 92, 219

Han, H.-J., Lu, X.-P., Yang, Y.-Z., Zhang, H., & Mutelo, A. M. 2020, RAA (Research in Astronomy and Astrophysics), 20, 129

Hapke, B. 1973, Moon, 7, 342

Hapke, B. 2001, J. Geophys. Res., 106, 10039

Hapke, B. 2005, Theory of Reflectance and Emittance Spectroscopy (Cambridge univ. press)

Head, J. W., & Wilson, L. 2017, Icarus, 283, 176

Hu, X., Ma, P., Yang, Y., et al. 2019, Geophys. Res. Lett., 46, 9439

Hunt, G. R. 1977, Geophysics, 42, 501

Ishii, T., McCallum, S., & Ghose, S. 1983, in Lunar and Planetary Science Conference Proceedings, 88, 631

Jiang, T., Zhang, H., Yang, Y., et al. 2019, Icarus, 331, 127

Keller, L. P., & McKay, D. S. 1993, Science, 261, 1305

Klima, R. L., Pieters, C. M., & Dyar, M. D. 2007, Meteoritics and Planetary Science, 42, 235

Klima, R. L., Pieters, C. M., & Dyar:, M. D. 2008, Meteoritics and Planetary Science, 43, 1591

Klima, R. L., Pieters, C. M., Boardman, J. W., et al. 2011, Journal of Geophysical Research (Planets), 116, E00G06

Lauretta, D. S., Dellagiustina, D. N., Bennett, C. A., et al. 2019, Nature, 568, 55

Le Corre, L., Reddy, V., Sanchez, J. A., et al. 2015, Icarus, 258, 483

Lindsay, S. S., Marchis, F., Emery, J. P., Enriquez, J. E., & Assafin, M. 2015, Icarus, 247, 53

Lindsley, D. H. 1983, American Mineralogist, 68, 477

Loeffler, M. J., Dukes, C. A., & Baragiola, R. A. 2009, Journal of Geophysical Research (Planets), 114, E03003

Lucey, P. G. 2004, Geophys. Res. Lett., 31, L08701

Mustard, J. F., Poulet, F., Gendrin, A., et al. 2005, Science, 307, 1594

Noble, S. K., Pieters, C. M., Hiroi, T., & Taylor, L. A. 2006, Journal of Geophysical Research (Planets), 111, E11009

Ohtake, M., Matsunaga, T., Haruyama, J., et al. 2009, Nature, 461, 236

Pieters, C. M., & Mustard, J. F. 1988, Remote Sensing of Environment, 24, 151

Pieters, C. M., Fischer, E. M., Rode, O., & Basu, A. 1993, J. Geophys. Res., 98, 20817

Pieters, C. M., Taylor, L. A., Noble, S. K., et al. 2000, Meteoritics and Planetary Science Supplement, 35, A127

Pieters, C. M., Boardman, J., Buratti, B., Chatterjee, A., & White, M. 2009, Current Science, 96, 500

Pinet, P. C., Glenadel-Justaut, D., Daydow, Y., et al. 2016, in 2016 8th Workshop on Hyperspectral Image and Signal Processing: Evolution in Remote Sensing (WHISPERS), IEEE, 1

Potin, S., Manigand, S., Beck, P., Wolters, C., & Schmitt, B. 2020, Icarus, 343, 113686

Poulet, F., Ruesch, O., Langevin, Y., & Hiesinger, H. 2015, Icarus, 253, 364

Roush, T. L., Bishop, J. L., Brown, A. J., Blake, D. F., & Bristow, T. F. 2015, Icarus, 258, 454

Sasaki, S., Nakamura, K., Hamabe, Y., Kurahashi, E., & Hiroi, T. 2001, Nature, 410, 555

Savitzky, A., & Golay, M. J. E. 1964, Analytical Chemistry, 36, 1627

Shirley, K. A., & Glotch, T. D. 2019, Journal of Geophysical Research (Planets), 124, 970

Singer, R. B. 1981, J. Geophys. Res., 86, 7967

Staid, M. I., Pieters, C. M., Besse, S., et al. 2011, Journal of Geophysical Research (Planets), 116, E00G10

Sunshine, J. M., Bus, S. J., McCoy, T. J., et al. 2004, Meteoritics and Planetary Science, 39, 1343

Sunshine, J. M., & Pieters, C. M. 1993, J. Geophys. Res., 98, 9075

Sunshine, J. M., & Pieters, C. M. 1998, J. Geophys. Res., 103, 13675

Sunshine, J. M., Pieters, C. M., & Pratt, S. F. 1990, J. Geophys. Res., 95, 6955

Thomas, C. A., Emery, J. P., Trilling, D. E., et al. 2014, Icarus, 228, 217

Thomas, P. C., Parker, J. W., McFadden, L. A., et al. 2005, Nature, 437, 224

Tsuda, Y., Saiki, T., Terui, F., et al. 2020, Acta Astronautica, 171, 42

Vernazza, P., Binzel, R. P., Thomas, C. A., et al. 2008, Nature, 454, 858

Wells, P. R. A. 1977, Contributions to Mineralogy and Petrology, 62, 129

Yamada, M., Sasaki, S., Nagahara, H., et al. 1999, Earth, Planets, and Space, 51, 1265

Yang, Y., Zhang, H., Wang, Z., et al. 2017, A&A, 597, A50

Zaini, N., van der Meer, F., & van der Werff, H. 2014, Remote Sensing, 6, 4149

Zambon, F., De Sanctis, M. C., Schröder, S., et al. 2014, Icarus, 240, 73

Zhang, H., Yang, Y., Jin, W., Liu, C., & Hsu, W. 2014, Optics Express, 22, 21280

Zhang, H., Yang, Y., Yuan, Y., et al. 2015, Geophys. Res. Lett., 42, 6945